Microsc. Microanal. 21, 498–509, 2015
doi:10.1017/S1431927614013592

Microscopy AND Microanalysis

Investigation of (Fe,Co)NbB-Based Nanocrystalline Soft Magnetic Alloys by Lorentz Microscopy and Off-Axis Electron Holography

Changlin Zheng,[1,†] Holm Kirmse,[1] Jianguo Long,[2] David E. Laughlin,[2] Michael E. McHenry,[2] and Wolfgang Neumann[1,3,*]

[1]*Institute of Physics, Humboldt University of Berlin, D-12489 Berlin, Germany*
[2]*Department of Materials Science and Engineering, Carnegie Mellon University, Pittsburgh, PA 15213, USA*
[3]*Department of Chemistry, University of Oregon, Eugene, OR 97403, USA*

Abstract: The relationship between microstructure and magnetic properties of a (Fe,Co)NbB-based nanocrystalline soft magnetic alloy was investigated by analytical transmission electron microscopy (TEM). The microstructures of $(Fe_{0.5}Co_{0.5})_{80}Nb_4B_{13}Ge_2Cu_1$ nanocrystalline alloys annealed at different temperatures were characterized by TEM and electron diffraction. The magnetic structures were analyzed by Lorentz microscopy and off-axis electron holography, including quantitative measurement of domain wall width, induction, and *in situ* magnetic domain imaging. The results indicate that the magnetic domain structure and particularly the dynamical magnetization behavior of the alloys strongly depend on the microstructure of the nanocrystalline alloys. Smaller grain size and random orientation of the fine particles decrease the magneto-crystalline anisotropy and suggests better soft magnetic properties which may be explained by the anisotropy model of Herzer.

Key words: TEM, electron holography, Lorentz microscopy, soft magnetic alloy, nanocrystalline

Introduction

Nanocrystalline soft magnetic materials have attracted considerable interest due to their excellent magnetic properties and have been proposed or used for a variety of soft magnetic devices from transformers to inductive devices (Yoshizawa et al., 1988; Herzer, 1992; McHenry et al., 1999*a*, 1999*b*; Long et al., 2008; Herzer, 2013). Most of the nanocrystalline soft magnetic systems are composed of a two-phase structure where randomly oriented nanoparticles with an average size from several to several tens of nanometers are dispersed in an amorphous matrix. Structural and compositional variation on the nanoscale strongly affects the magnetic properties, especially the extrinsic ones including magnetic permeability and coercivity (McHenry et al., 1999*b*). Further optimization of the magnetic properties requires understanding of the physical origin of magnetic behavior, particularly the existing relationship between microstructure and magnetic domain structure in soft magnetic nanocrystalline alloys. FeCo-based nanocomposites are particularly important because the large exchange interactions in FeCo (MacLaren et al., 1999) and strong distributed exchange interactions in FeCo-based amorphous phases (Gallagher et al., 1999) as compared with Fe-based nanocomposites, influence micromagnetic parameters and Fe-Co pair correlations that can be responsible for field (Johnson et al., 2006) and strain-induced anisotropies (Ohodnicki et al., 2010; Shen et al., 2014).

Lorentz microscopy (Hale et al., 1959; Chapman, 1984; De Graef, 2001; Beleggia & Zhu, 2005) and electron holography (Tonomura, 1999; Shindo & Oikawa, 2002; Lichte et al., 2007; McCartney & Smith, 2007; Lichte & Lehmann, 2008; Snoeck et al., 2008; Dunin-Borkowski et al., 2012) are analytical transmission electron microscopy (TEM) techniques used to study the local magnetization state of materials. When high energy electrons are transmitted through a magnetic sample in a TEM, the magnetic vector potential of the sample will cause an additional phase shift of the electrons. The phase shift of the electrons could be further transferred into amplitude contrast to reveal the magnetic domain structure directly under certain conditions (like defocus imaging in Fresnel mode Lorentz microscopy, see Figs. 1a–1c) or imaged by electron holography (Fig. 1d). Compared with other experimental techniques commonly used for studying the magnetic properties of materials like magneto-optical Kerr effect measurements (Argyle & Terrenzio, 1984), magnetic force microscopy (Martin & Wickramasinghe, 1987; Saenz et al., 1987), spin-polarized scanning tunneling microscopy, and scanning electron microscopy with polarization analysis, Lorentz microscopy and electron holography provide a high spatial resolution of magnetic imaging on a nm scale. Furthermore, they can also be combined with other advanced TEM imaging, diffraction, and spectroscopy techniques to examine microstructure and microchemistry of materials at atomic resolution. This is a

Received June 24, 2014; accepted October 24, 2014
*Corresponding author. wolfgang.neumann@physik.hu-berlin.de
†Current address: Monash Centre for Electron Microscopy, Monash University, Victoria 3800, Australia

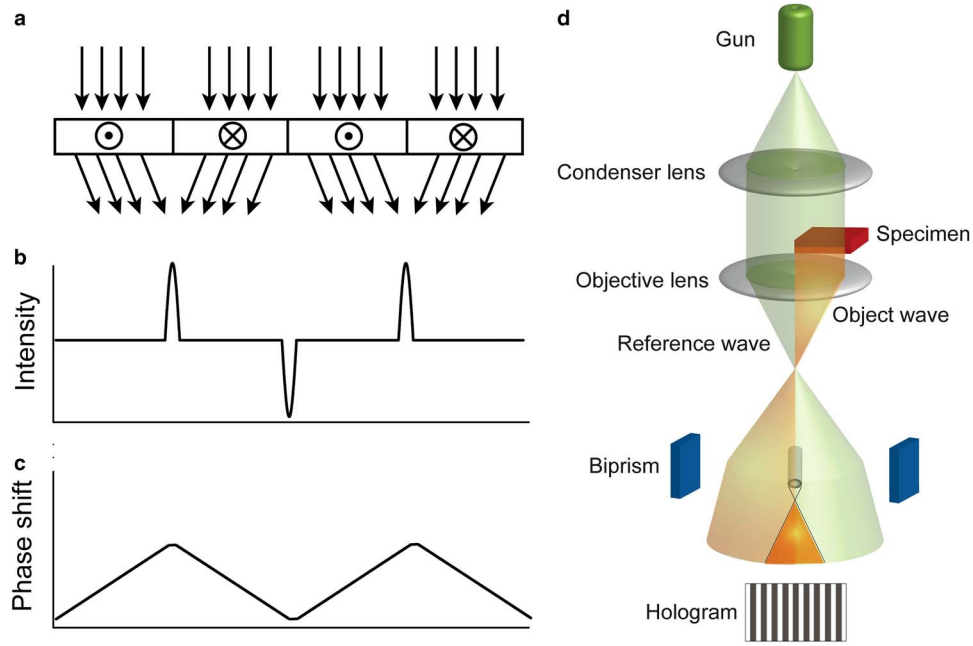

Figure 1. Schematic illustration of the formation of magnetic contrast in transmission electron microscopy (TEM). (**a**) Deflection of electron beam by Lorentz force in different magnetic domains. (**b**) Intensity distribution of electrons at a certain distance below the exit plane of the specimen (Fresnel mode). (**c**) Phase shift of electrons at the exit plane of the specimen. (**d**) Principle of off-axis electron holography.

unique benefit for the study of relationships between microstructure and magnetic domain structure in nanocrystalline soft magnetic alloys. High resolution TEM (Hiraga & Kohmoto, 1991) and electron holography (Shindo et al., 2002) have been applied to the study of nanocrystalline systems such as FINEMET (Yoshizawa et al., 1988). In this work, we use specific TEM methods to study structure-property correlations in the novel (Fe,Co)NbB nanocrystalline softmagetic alloy system.

Materials and Methods

The (Fe,Co)NbB-based nanocrystalline alloys were fabricated in a two-step procedure. First, an amorphous ribbon (30 μm thickness, ~3 mm width) with nominal composition $(Fe_{0.5}Co_{0.5})_{80}Nb_4B_{13}Ge_2Cu_1$ was prepared by single roller melt spinning. Second, the amorphous samples were crystallized by annealing at 550 and 610°C, respectively, for 1 h and subsequently quenched to room temperature by water (Long et al., 2007). Previous investigations showed that this alloy system exhibited magnetic properties comparable with those of commercially available materials (Long et al., 2008). Plan-view samples were prepared by final ion milling for TEM investigation. All TEM investigations were performed on a JEOL JEM-2200FS field emission electron microscope operated at 200 kV. For Lorentz microscopy and electron holography experiments, the objective lens was turned off and an objective mini lens below the lower pole piece of the objective lens was used for imaging to keep the sample in a magnetic field-free environment. The microscope had an electron biprism (platinum wire of 600 nm diameter) located close to the selected area aperture plane for electron holography experiments. A biprism voltage 70–80 V was applied in Lorentz mode, the hologram fringe spacing was 10–11.5 nm, and the width of the hologram was 2.5–3 μm. The electron holograms were recorded with a Gatan 794 slow scan CCD camera. Further processing and reconstruction of the holograms were carried out by the "Holoworks" package of Gatan's Digital Micrograph software. In addition, an in-column energy filter was utilized in scanning transmission electron microscopy (STEM) mode for measuring electron energy-loss spectra (EELS) to determine the sample thickness.

Results and Discussion

Structural Characterization

The structure and morphology of the alloys annealed at different temperatures were investigated by TEM, selected area electron diffraction (SAED) and nano-beam electron diffraction (NBED). Figure 2a shows a bright-field (BF)-TEM image of a $(Fe_{0.5}Co_{0.5})_{80}Nb_4B_{13}Ge_2Cu_1$ sample annealed at 550°C for 1 h. It is obvious that some small particles are dispersed in the matrix. The size of the grains is in the range of 10–30 nm with an average grain size of 17.5 ± 4.0 nm. The compositional segregation of Fe and Co elements in the grains was proven by three-dimensional atom probe (3DAP) analysis (Ping et al., 2001; Long et al., 2007).

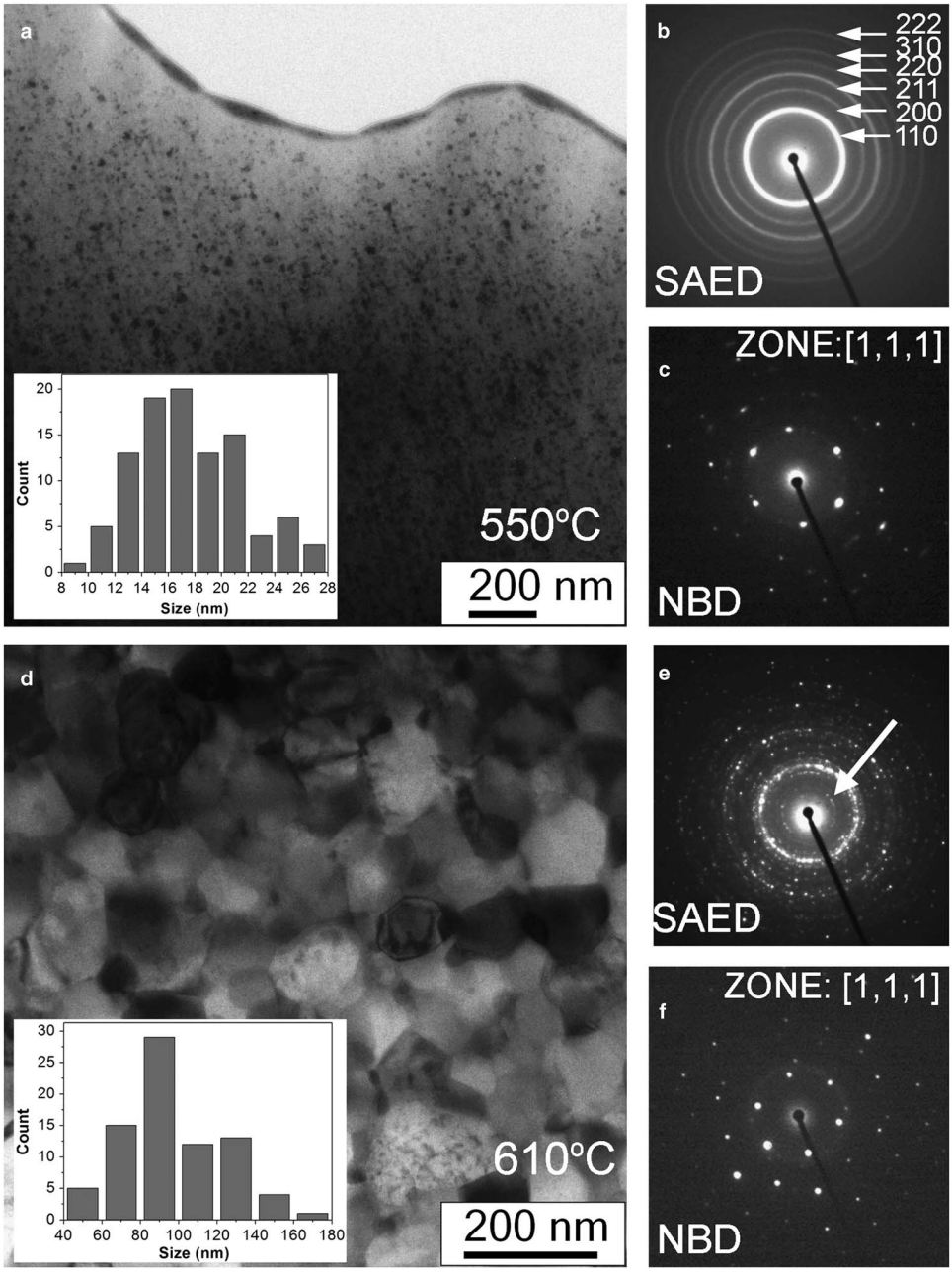

Figure 2. (**a**) Bright-field transmission electron microscopy (BF-TEM) image of a (Fe,Co)NbB-based nanocrystalline alloy annealed at 550°C for 1 h. Insert: a magnified region of the alloy. (**b**) Selected area electron diffraction (SAED) pattern, (**c**) nano-beam electron diffraction (NBED) pattern from a single nanoparticle, (**d**) High-angle annular dark-field (HAADF) image of a (Fe,Co)NbB based nanocrystalline alloy annealed at 610°C for 1 h, (**e**) SAED pattern, (**f**) NBED pattern.

Figure 2b shows a SAED pattern taken from a large area including lots of grains embedded in the matrix. The Debye-Scherrer rings indicate that the nanocrystalline grains are randomly oriented. Each peak of the rings could be indexed as α-FeCo (bcc structure) with a lattice parameter of 2.85 Å. The wide halo-ring overlapping the (110) ring indicates that there is a large residual amorphous phase in the alloy. The NBED pattern (Fig. 2c) of an individual nanocrystalline grain shows a typical diffraction pattern of a single crystal, which could be indexed as α-FeCo phase in the [111] orientation. Some out of zone axis NBED patterns were also observed which indicates an out of plane random orientation. Both SAED and NBED prove that the alloy consists of randomly oriented single crystalline FeCo particles.

The BF-TEM image (Fig. 2d) indicates an increase in grain size to 96 ± 26 nm for the sample annealed at 610°C. The grains have an irregular sharp shape and are very closely clustered to each other. This indicates that most of the residual amorphous phase is recrystallized to the nanocrystalline phase. The Debye-Scherrer rings in the SAED pattern (Fig. 2e)

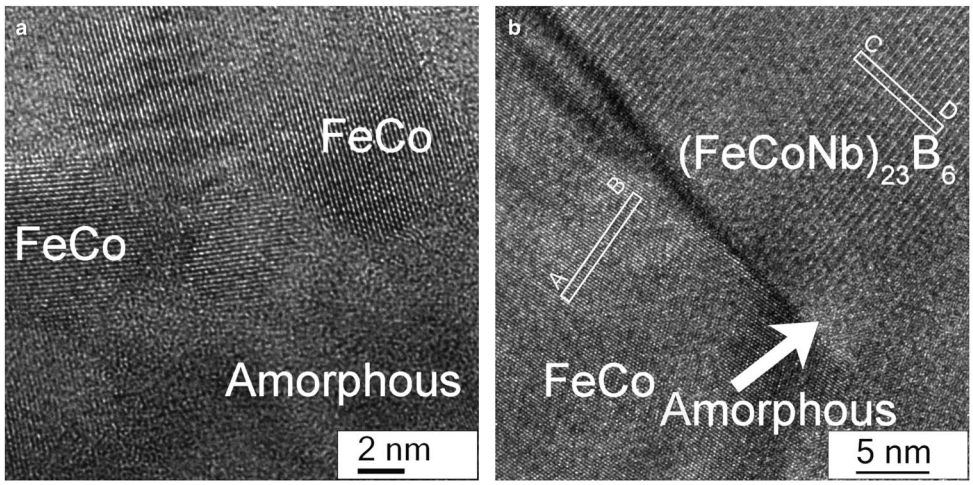

Figure 3. High-resolution transmission electron microscopy (HRTEM) images of a (Fe,Co)NbB-based nanocrystalline alloy annealed at different temperatures for 1 h. (**a**) 550°C, (**b**) 610°C.

confirm that the grains are still randomly oriented. However, the rings look more discrete which again reveals the larger grain size. The disappearance of the halo ring in the SAED pattern evidences a strong reduction of the residual amorphous phase. Though most of the Debye-Scherrer rings correspond to the α-FeCo phase, several diffraction spots could be found surrounding the primary beam as marked by the arrow. These diffraction spots correspond to the fcc $(Fe,Co,Nb)_{23}B_6$ phase which has a large lattice parameter ($a = 10.9$ Å). This phase indicates that secondary crystallization has already taken place at the higher annealing temperature of 610°C (Long et al., 2007).

High-resolution transmission electron microscopy (HRTEM) studies were carried out to obtain more information about the microstructure of the alloys at an atomic level of magnitude. Figure 3a shows a HRTEM image of the sample heated at 550°C for 1 h. Several small nanocrystalline grains with lattice fringe contrast could be seen surrounded by the amorphous phase with maze contrast. Those grains have different orientations, but the two sets of lattice fringes were measured as 2.0 Å. This corresponds to the (110) interplanar spacing of the α-FeCo phase and is in good agreement with the electron diffraction results.

The HRTEM image of an alloy annealed at 610°C for 1 h is shown in Figure 3b. Only a very small part of the amorphous phase could be found among the boundaries of the grains. The averaged fringe spacing along the line AB in the left bottom grain is 2.1 ± 0.1 Å, which approves the grain crystallizes in the α-FeCo phase. On the contrary, the average fringe spacing along the line CD in the top right grain is much larger (5.5 ± 0.1 Å), and it corresponds to the (002) interplanar spacing of $Fe_{23}B_6$-type phase (with lattice constant 10.9 Å).

Investigation of the Magnetic Domain Structure

The magnetic domain structure of the alloys was investigated by Lorenz microscopy and electron holography. Figure 4 shows Lorenz microscopy images and the corresponding reconstructed phase image of the off-axis hologram of an alloy sample annealed at 550°C for 1 h. The in-focus Lorentz microscopy image of Figure 4a looks like a conventional bright-field image where only structural features, but no magnetic contrast is visible. When the imaging condition was changed from in-focus to over focused, several Fresnel fringes could be seen at the edge of the sample due to the large defocus. The bright and dark lines indicate the positions of domain walls (Fig. 4b). The size of the magnetic domains is on the order of several hundred nanometers (with an average size of 560 ± 190 nm), which is much larger than the average grain size of the nanocrystallites (17.5 ± 4.0 nm). Figure 4c shows the reconstructed phase image of an off-axis electron hologram from the same area. The phase image shows a series of black and dark phase contour lines that directly image the magnetic flux within the sample. The spacing of the contour lines is 2π corresponding to a magnetic flux $h/e = 4.1 \times 10^{-15}$ Wb between the adjacent contour lines. The vortex structures in the phase image are formed by the changes of magnetization in adjacent domains while the vortex center is the cross point of several adjacent domain walls. The closure of the vortex structure is an indication that the sample has a very weak magnetic anisotropy. The contour line spacing is nearly uniform in most parts of the image indicating a uniform magnetic flux density. Close to the lower end of the peninsula, the contour line spacing is broadened because the phase gradient is reduced to 15 ± 1 rad/μm caused by a lower sample thickness in this area. Around the sample the leakage field can also be found in the vacuum.

Though the raw phase image shows a detailed distribution of the magnetic flux, it is difficult to distinguish the individual magnetic domains from it. Therefore the directions of magnetic flux were calculated and color coded mapped. First, the raw phase image of Figure 4c was unwrapped to remove the 2π phase jump, then the directions of maximal phase gradient at each pixel position were calculated and further rotated by 90° (the directions of magnetic flux are

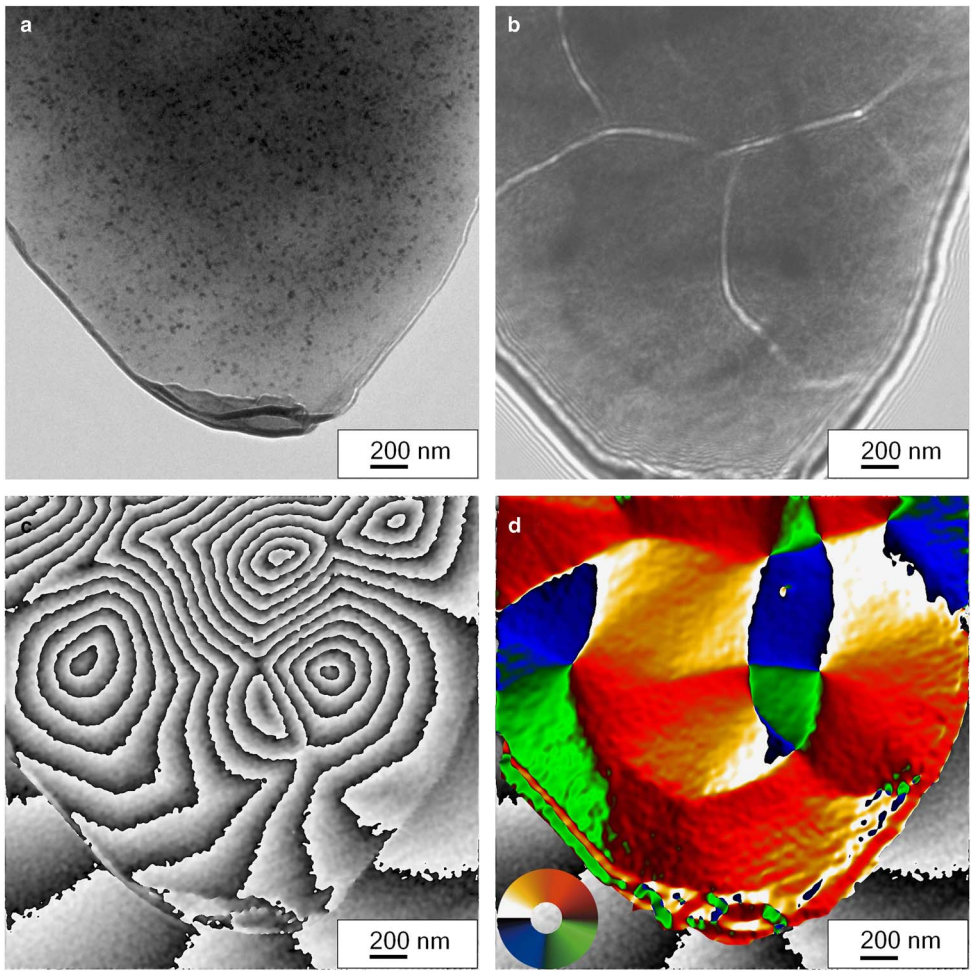

Figure 4. Magnetic domain structures of (Fe,Co)NbB-alloy annealed at 550°C. In focus (**a**) and under focus (**b**) Lorentz microscopy images. Reconstructed phase image of off-axis electron hologram (**c**), Color-coded mapping of magnetic flux directions (**d**). The magnetization direction is indicated by the inserted color plate.

perpendicular to the directions of maximal phase gradient). The different magnetic domains are clearly distinguished in the mapped color-coded magnetic flux directions (Fig. 4d). It can be clearly seen that most of the domain walls are close to a 90° type rather than to a 180° type.

Lorentz microscopy images and the corresponding reconstructed phase image of the off-axis electron hologram of an alloy sample annealed at 610°C for 1 h are shown in Figure 5. Quite different from the sample annealed at 550°C where the average magnetic domain size is in the range of 560 ± 190 nm, the size of the magnetic domains is significantly smaller for 610°C. The average magnetic domain size is in the range of 210 ± 70 nm. Each of the magnetic domains consists of only two or three crystal grains (Fig. 5b). The distribution of the domain sizes of two samples are compared in Figure 6. The reconstructed phase image (Fig. 5c) shows that the magnetic flux in this sample is very complex and disordered, which hints to poor soft magnetic properties.

The width of the magnetic domain walls of the alloy sample annealed at 550°C was further measured by means of defocus series of Lorentz microscopy images (Fig. 7). Though the domain wall has a certain width, it does not show any contrast under in-focus condition in Lorentz microscopy since the magnetic field is a pure phase object for high-energy electrons. Therefore, the domain wall width has to be determined by fitting the wall widths measured at different defocus settings. The under- and over-focus series of Lorentz microscopy images of a typical magnetic domain wall of an alloy sample annealed at 550°C are shown in Figures 7a and 7b, respectively. In the over-focused images with convergent electrons, several interference fringes can be seen due to the coherent interference of deflected beams from adjacent domains. In order to improve the accuracy, the wall width was only determined from divergent domain wall images. The linear fit of the plotted wall widths as a function of defocus values is shown in Figure 7c. The domain wall width estimated from this curve is 45 ± 3 nm (linear extrapolation to zero-defocus) which is much larger than the average grain size of 17.5 ± 4.0 nm.

The magnetic flux density was also quantitatively measured by electron holography. The phase of beam electrons modified by the electrostatic and magnetic field could be

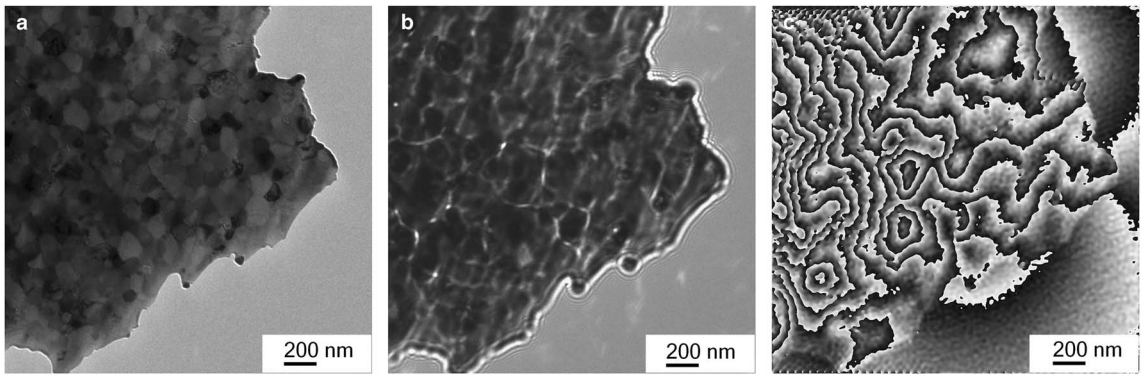

Figure 5. Magnetic domain structure of a (Fe,Co)NbB-based alloy annealed at 610°C for 1 h. In focus (**a**) and under focus (**b**) Lorentz microscopy images. (**c**) Reconstructed phase image of off-axis electron hologram.

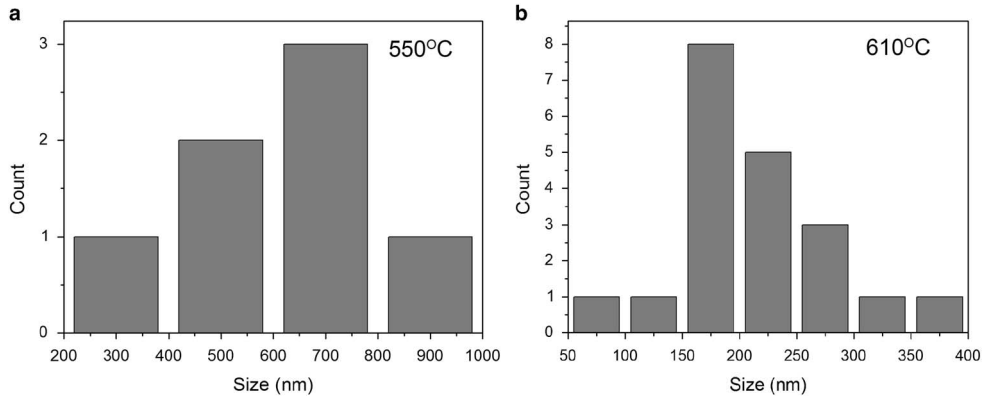

Figure 6. Distribution of the magnetic domain size of the samples annealed at 550°C (**a**) and 610°C (**b**).

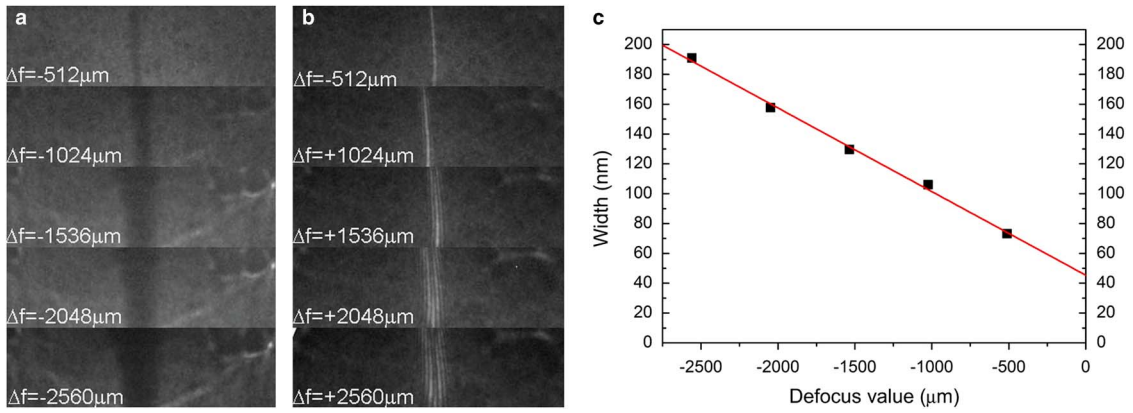

Figure 7. Defocus series of Lorentz microscopy images of a (Fe,Co)NbB-based alloy annealed at 550°C. Divergent contrast (**a**) and convergent contrast images (**b**), measured domain wall width from convergent contrast images, straight line – linearly fitted wall width as a function of defocus value (**c**).

written as (Tonomura, 1999; Lichte et al., 2007; McCartney & Smith, 2007; Lichte & Lehmann, 2008):

$$\varphi(x) = C_E \int V_0(x,z)dz - \frac{e}{\hbar}\iint B_n(x)dxdz \qquad (1)$$

where C_E is the interaction constant, V_0 the crystal mean inner Coulomb potential (MIP), e the electron charge, $\hbar$ the reduced Planck constant, B_n the magnetic flux density perpendicular to the beam direction. Particularly in the area with homogenous thickness the Coulomb potential contribution to the phase gradient will be zero. Then the magnetic flux density B is determined by:

$$B = -\left(\frac{\hbar}{et}\right)\frac{d\phi}{dx} \qquad (2)$$

where $d\phi/dx$ is the magnitude of the phase gradient of electrons perpendicular to the x direction. The thickness of

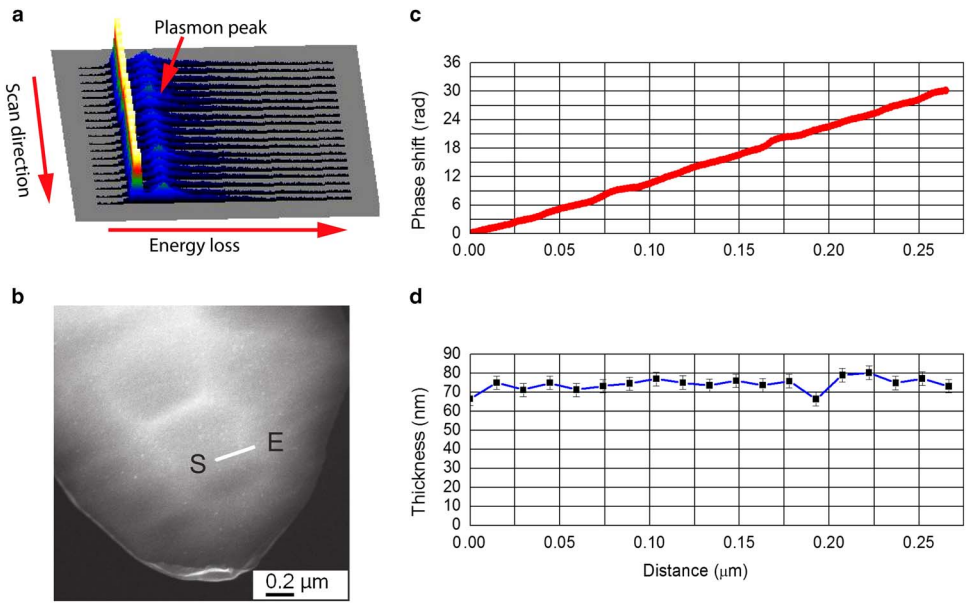

Figure 8. (**a**) Electron energy-loss spectra (EELS) line scan spectra of a (Fe,Co)NbB-based alloy annealed at 550°C for 1 h. (**b**) Scanning transmission electron microscopy high-angle annular dark-field (STEM-HAADF) image (S – E path of line scan profile). (**c**) corresponding unwrapped phase line profile along path S – E. (**d**) thickness line profile retrieved from EELS spectra.

the sample was independently determined by EELS measurements by means of the log-ratio method (Egerton, 1996).

To measure the magnetic flux density, the phase image as shown in Figure 4d was unwrapped to remove the phase jump at 2π. Then a phase line profile was taken along the maximal phase gradient direction within a single domain. Subsequently, an EELS line scan (Fig. 8a) was taken in STEM mode (Fig. 8b) along the same path. The thickness of the sample was calculated by log-ratio method from the spectrum. The line profile of the electron phase shift and the corresponding thickness profile are compared in Figures 8c and 8d. The phase shift is linear along the path from S to E with a gradient of 101.9 rad/μm. The thickness profile measured from EELS along the same path (Fig. 8d) is nearly uniform with an average thickness of 74 ± 5 nm. Therefore the contribution of MIP to the relative phase shift could be neglected. The magnetic flux density B was calculated as 1.0 ± 0.1 T, according to equation 2.

Dynamic Magnetization Processes in Applied Field

As already mentioned for structure investigations of magnetic domains in TEM the objective lens is normally switched off. When the objective lens is slightly excited and the sample is tilted, an in-plane component of the objective lens field is introduced to the object plane. The strength of the in plane component of the field depends on the tilting angle θ:

$$H_{//} = H \sin(\theta) \tag{3}$$

This residual field can be used as an applied field to study the dynamic magnetic behavior of the alloys (Fig. 9).

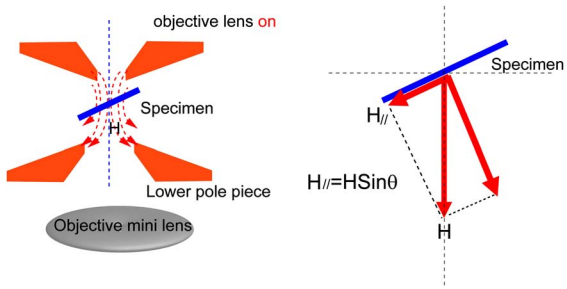

Figure 9. Schematic illustration introducing an in-plane applied magnetic field by tilting the sample.

Figure 10 shows the tilting series of the Lorentz microscopy images of the sample annealed at 550°C. The objective lens was only slightly excited to 0.78% of the maximum lens current which corresponds to a magnetic field H of 156 Oe at the sample position. The direction of the in-plane component of the applied field is indicated by the arrows in the first image. The tilting angles were read out from the goniometer and marked on each of the images. The zero in-plane field is not coincident with the sample position for a zero-degree tilting angle read out from the goniometer, which is due to the ion-milling prepared wedged shape of the sample.

When the tilting angle was initially set to 15°, very few and weak domain walls can be seen. This indicates that most of the magnetizations were aligned along the $H_{//}$ (the in-plane applied field). While the strength of $H_{//}$ has been further decreased by decreasing the tilting angle, more and more magnetic domain walls are visible forming the domain structure. When the sample was tilted to 5.3° most of the

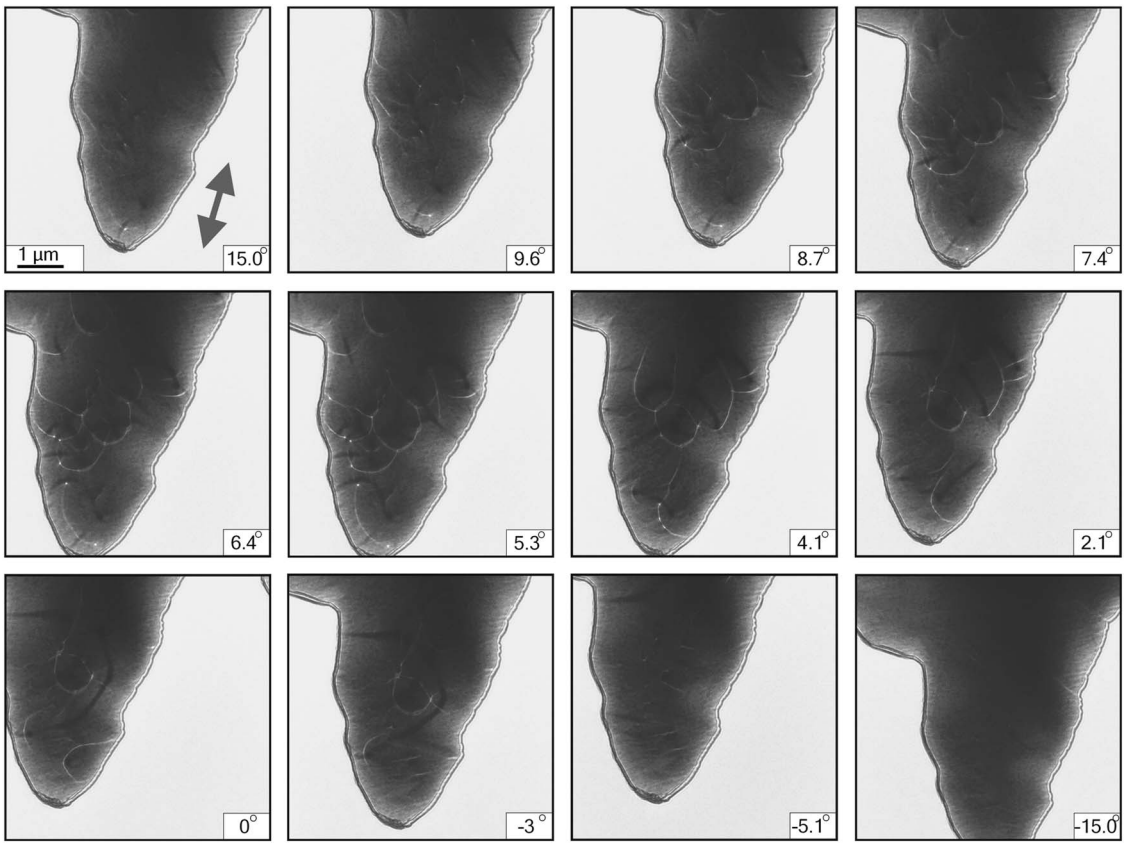

Figure 10. Tilt series of Lorentz microscopy images of a (Fe,Co)NbB-based nanocrystalline alloy annealed at 550°C for 1 h. The directions of the in-plane component of the applied field are schematically illustrated in the upper left image by arrows.

magnetic domains walls could be seen. This indicates that the in-plane field direction has already been reversed and the field magnitude is close to the coercivity field H_c.

With further tilting, the small magnetic domains began to emerge into larger domains due to the increased $H_{//}$ in the opposite direction. The domain wall motion was also observed in this process. Particularly during continuous tilting of the sample, which also means a continuous change of $H_{//}$, the motion of the domain walls was not continuous, but had sudden jumps from one position to another. This is a clear reflection of the Barkhausen effect (Barkhausen, 1919; Alessandro et al., 1990*a*, 1990*b*) at the microscopic scale. The Barkhausen noise is caused by the abrupt change of the domain configuration due to the pinning of domain walls. After further tilting to −5.1°, the domain wall disappeared. This indicates that the sample was in the saturation state there was no change with further tilting. From the series of tilt images it can be seen that the sample can be easily magnetized and demagnetized even at a small $H_{//}$ (maximal 40 Oe at 15° tilting).

A tilt series of reconstructed phase images off-axis electron holograms (Fig. 11) provides more detail about the change of the magnetic flux. At the initial tilting angle of 19.8° most of the magnetic flux was forced along the applied field direction and only a small vortex structure was left at the bottom right. With decreasing tilting angle (decreasing $H_{//}$), the vortex began to grow which indicates that more and more magnetic flux around the vortex center turned away from $H_{//}$. At the upper part of the images several other vortexes were formed. When the sample was tilted close to 4.8°, the vortexes grew to the maximum. If we followed the magnetic flux around the vortex center, we found that the magnetic flux density which was indicated by the phase contour line spacing is nearly the same (neglecting the thickness effect). The magnetic flux with opposite directions cancels each other out. This state is close to the zero net flux in the hysteresis loop and the strength of $H_{//}$ is close to the coercivity force H_c.

Since the direction of $H_{//}$ was inverted with increased tilting, the vortex began to shrink which indicated that the magnetic flux partly turned to the applied field direction. At a tilting angle of −5.0°, the complete magnetic flux was aligned along the direction of the $H_{//}$, and the domain structures disappeared which corresponds to the saturation state in the hysteresis loop. With additional tilting, no changes were observed. In order to observe the change of the magnetic domain configurations during the magnetization, the direction of the magnetic flux was calculated from the phase images in Figure 11. The result of the color coded flux directions is shown in Figure 12 where the different magnetic

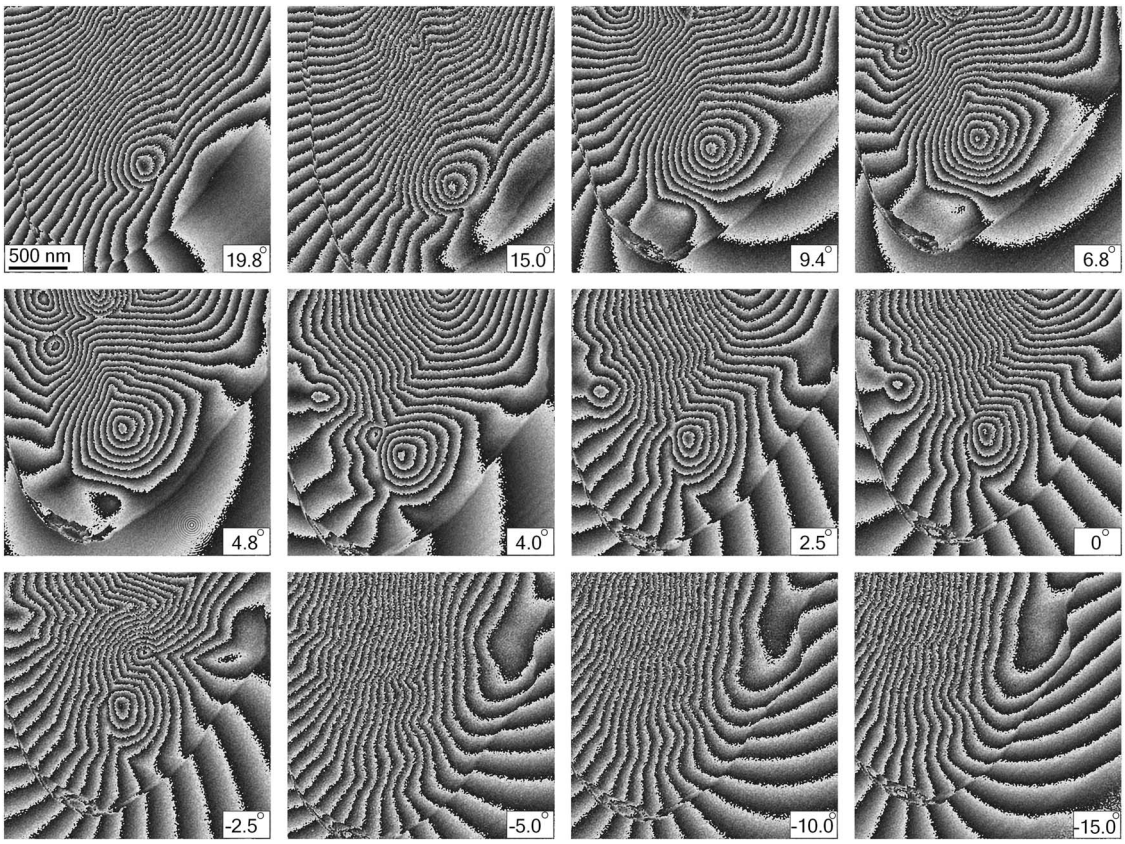

Figure 11. Tilt series of reconstructed phase images of off-axis electron holograms of a (Fe,Co)NbB-based nanocrystalline alloy annealed at 550°C for 1 h.

domains and flux directions inside the domains can be seen. From the first image at a tilting angle of 19.8°, it can be seen that the sample consists of a large red zone with a uniform magnetization, except for several very small adjacent domains (yellow, blue, and green color regions) in forming the vortex structure. With the decreased applied field $H_{//}$, those small domains began to grow. It is very interesting to note that during domain growth, the relative position of the boundary between the small domains did not change so each of the domains was only expanded to the matrix independently and formed the larger domains. At a tilting angle of 4.8°, the domains grew to the maximum. As we have mentioned, the applied field was close to the coercivity field. Between the two images of 4.8 and 4.0°, the domain configurations show a significant change. As we have observed in Lorentz microscopy, this kind of change is again due to the sudden jump of the domain walls under the increased applied in-plane field. Finally, the domain structure disappeared. Now the whole sample is magnetized along the blue direction that is opposite to the initial red direction.

As discussed by Pozzi (2002), modulation of the reference wave has a significant effect on the electron holography experiments with long-range electromagnetic fields. For those electron holograms recorded close to the natural magnetization (no external applied field), the magnetic domains form closure structures. The stray field into the vacuum is weak. While an external field is applied and the magnetic flux is aligned along one direction, the stray field may be largely extended which affects the reference wave. In this dynamical magnetization experiment, the hologram fringes are aligned closer to the parallel direction of the applied field rather than perpendicular to it, so the stray field effect on the reference wave is reduced (Pozzi, 2002). In future experiments, the stray field problem may be solved using the recently developed "split illumination electron holography" technique (Tanigaki et al., 2012), where the split reference wave can be set far from the sample edge.

Figure 13 shows the tilting series of Lorentz microscopy images (upper row) and electron holography phase images (lower row) of the sample annealed at 610°C for 1 h with the same objective lens field. Contrary to the alloy samples annealed at 550°C, the configuration of the magnetic domains was not significantly changed with the change of the applied field. The domain walls were strongly pinned by grain boundaries. This indicates that the sample has a much higher coercivity. Similarly we can see in the phase images, though the sample was tilted to −15°, the magnetic flux is still disordered. No large homogenous domain can be seen. So the tilting series experiments indicate for samples annealed at 610°C that the coercivity is extremely high due to the strong pinning by the grain boundaries.

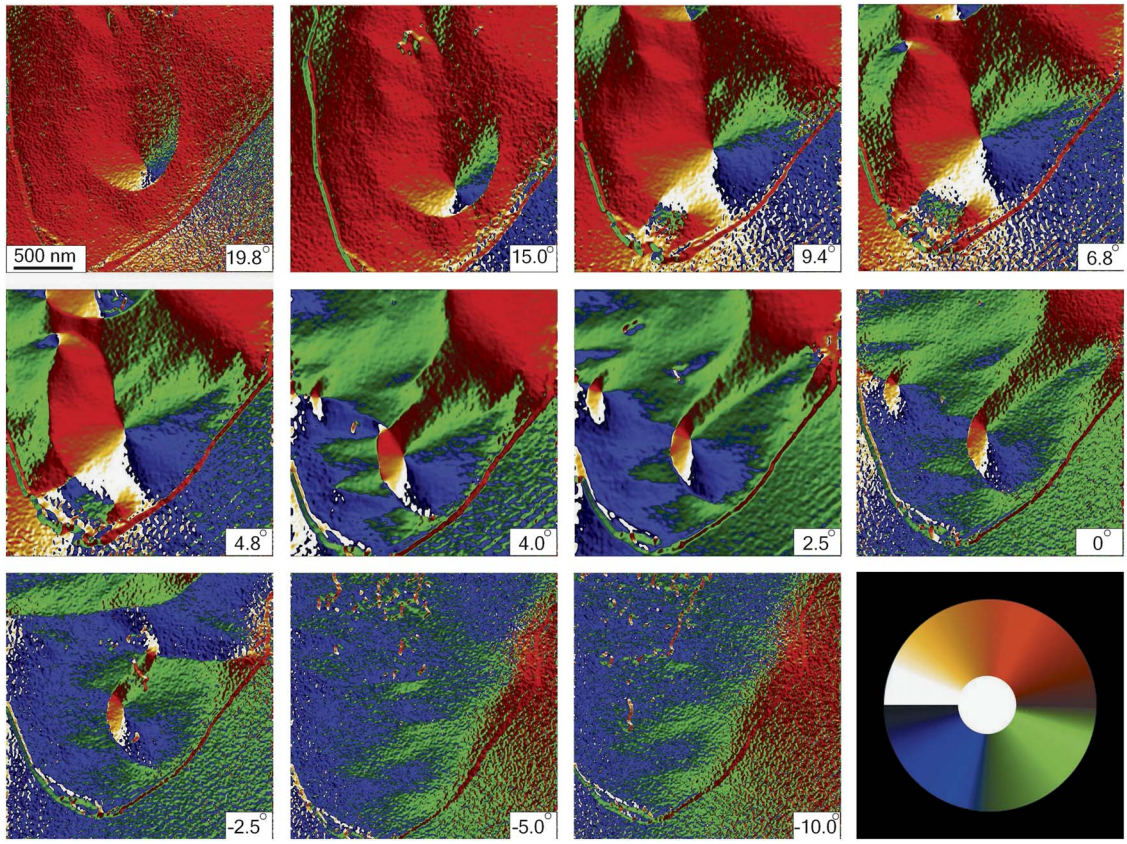

Figure 12. Color-coded mapping of magnetization of an (Fe,Co)NbB-based nanocrystalline alloy annealed at 550°C for 1 h. The directions of magnetization are represented by the inserted color plate.

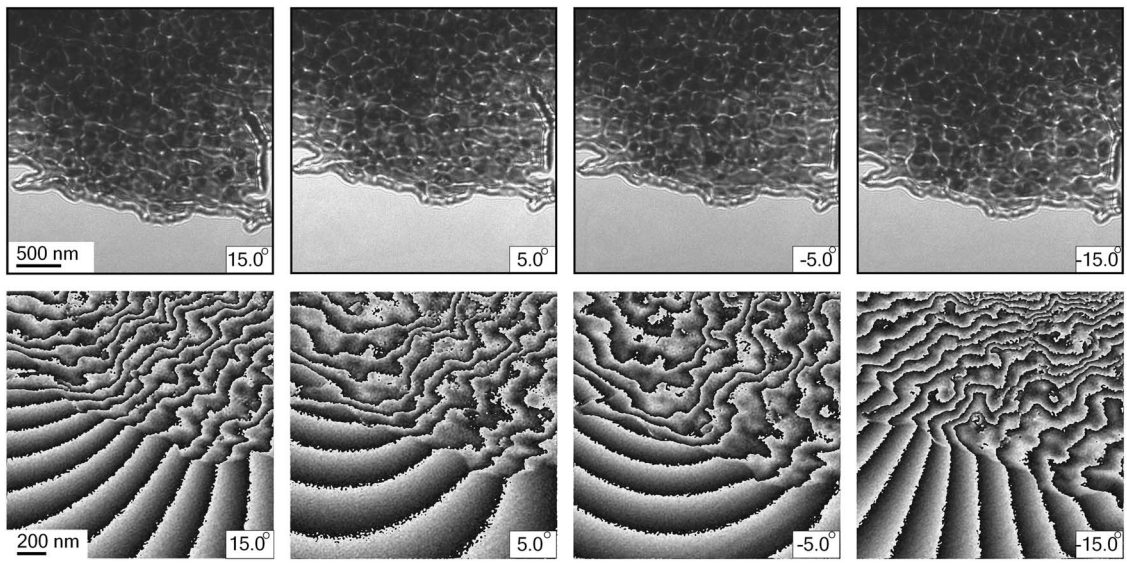

Figure 13. Tilt series of Lorentz microscopy (upper row) and electron holography (lower row) images of a (Fe,Co)NbB-based nanocrystalline alloy annealed at 610°C for 1 h.

From both the tilting series of Lorentz microscopy images and the phase images of electron holography we can conclude that the alloy samples annealed at 550°C can easily be magnetized and demagnetized with very little pinning. This is consistent with the coercivity measurement by a vibrating sample magnetometer (VSM, 3.1 Oe for 550°C sample and 11.5 Oe for 610°C sample). This may be explained by means of the Herzer random anisotropy model

(Herzer, 1992, 1993, 1997, 2013). In the random anisotropy model, there is a critical scale which is given by the ferromagnetic exchange length which is in the order of the domain wall width. As we have measured, the domain wall width in (Fe,Co)NbB-based nanocrystalline alloys with smaller average grain size (17.5 ± 4.0 nm) is in the range of 40–50 nm. When the grain size is below the ferromagnetic exchange length, the randomly oriented FeCo grains are ferromagnetically coupled by exchange interactions through the interfacial amorphous matrix (Herzer, 1997). Thus, the effective magneto-crystalline anisotropy is significantly reduced due to the average effect. The magnetization will not follow the randomly oriented easy axis of magnetization of the individual grains, but is forced to align parallel by exchange interaction (Herzer, 1997). This is the reason that we have observed the large magnetic domains in the alloy systems with an average grain size of 17.5 ± 4.0 nm. On the contrary, in samples annealed at higher temperature the domain walls are strongly pinned at the grain boundaries causing a high coercivity.

Summary

We investigated the microstructure, domain structure and domain wall dynamics of $(Fe_{0.5}Co_{0.5})_{80}Nb_4B_{13}Ge_2Cu_1$ nanocrystalline softmagnetic alloys. The results show that the magnetic domain structure and dynamical magnetization behavior of the alloys strongly depend on the microstructure of the nanocrystalline alloys and can be well explained by Herzer's anisotropy model.

Acknowledgment

The authors are thankful to Prof. H. Lichte (TU Dresden) and to Prof. M. Lehmann (TU Berlin) for valuable discussions. Ch. Z. appreciates very much the opportunity of having familiarized with the technique of off-axis electron holography at the Triebenberg Laboratory of Prof. H. Lichte. Ch. Z. greatfully acknowledges financial support from the German Science Foundation (DFG).

References

Alessandro, B., Beatrice, C., Bertotti, G. & Montorsi, A. (1990*a*). Domain-wall dynamics and Barkhausen effect in metallic ferromagnetic materials. 1. Theory. *J Appl Phys* **68**(6), 2901–2907.

Alessandro, B., Beatrice, C., Bertotti, G. & Montorsi, A. (1990*b*). Domain-wall dynamics and Barkhausen effect in metallic ferromagnetic materials. 2. Experiments. *J Appl Phys* **68**(6), 2908–2915.

Argyle, B.E. & Terrenzio, E. (1984). Magneto-optic observation of bloch lines. *J Appl Phys* **55**(6), 2569–2571.

Barkhausen, H. (1919). Zwei mit hilfe der neuen verstärker entdeckte erscheinugen. *Physik Zeitschrift* **20**, 401–403.

Beleggia, M. & Zhu, Y. (2005). Transmission electron microscopy. In *Modern Techniques for Characterizing Magnetic Materials*, Zhu, Y. (Ed.), pp. 267–326. Boston: Kluwer Academic Publishers.

Chapman, J.N. (1984). The investigation of magnetic domain-structures in thin foils by electron-microscopy. *J Phys D Appl Phys* **17**(4), 623–647.

De Graef, M. (2001). Lorentz microscopy: Theoretical basis and image simulations. In *Magnetic Imaging and Its Applications to Materials (Experimental Methods in the Physical Sciences, vol. 36)*, Graef, M.D. & Zhu, Y. (Eds.), pp. 27–67. San Diego: Academic Press.

Dunin-Borkowski, R.E., Kasama, T., Beleggia, M. & Pozzi, G. (2012). Lorentz microscopy and electron holography of magnetic materials. In *Handbook of Nanoscopy*, Tendeloo, G. V., Van Dyck, D. & Pennycook, S.J. (Eds.), pp. 221–252. Weinheim, Germany: Wiley-VCH.

Egerton, R.F. (1996). *Electron Energy-Loss Spectroscopy In The Electron Microscope*. New York: Plenum Press.

Gallagher, K.A., Willard, M.A., Zabenkin, V.N., Laughlin, D.E. & McHenry, M.E. (1999). Distributed exchange interactions and temperature dependent magnetization in amorphous $Fe_{88-x}CoxZr_7B_4Cu_1$ alloys. *J Appl Phys* **85**(8), 5130–5132.

Hale, M.E., Fuller, H.W. & Rubinstein, H. (1959). Magnetic domain observations by electron microscopy. *J Appl Phys* **30**(5), 789–791.

Herzer, G. (1992). Nanocrystalline soft magnetic-materials. *J Magn Magn Mater* **112**(1–3), 258–262.

Herzer, G. (1993). Nanocrystalline soft-magnetic materials. *Phys Scripta* **T49a**, 307–314.

Herzer, G. (1997). Nanocrystalline soft magnetic alloys. *Handb Magn Mater* **10**, 415–462.

Herzer, G. (2013). Modern soft magnets: Amorphous and nanocrystalline materials. *Acta Mater* **61**(3), 718–734.

Hiraga, K. & Kohmoto, O. (1991). Microstructure of Fe-Cu-Nb-Si-B soft magnetic-alloys studied by transmission electron-microscopy. *Mater T Jim* **32**(9), 868–871.

Johnson, F., Um, C.Y., McHenry, M.E. & Garmestani, H. (2006). The influence of composition and field annealing on magnetic properties of FeCo-based amorphous and nanocrystalline alloys. *J Magn Magn Mater* **297**(2), 93–98.

Lichte, H., Formanek, P., Lenk, A., Linck, M., Matzeck, C., Lehmann, M. & Simon, P. (2007). Electron holography: Applications to materials questions. *Annu Rev Mater Res* **37**, 539–588.

Lichte, H. & Lehmann, M. (2008). Electron holography - basics and applications. *Rep Prog Phys* **71**(1), 016102.

Long, J.G., McHenry, M., Urciuoli, D.P., Keylin, V., Huth, J. & Salem, T.E. (2008). Nanocrystalline material development for high-power inductors. *J Appl Phys* **103**(7), 07E705.

Long, J.G., Ohodnicki, P.R., Laughlin, D.E., McHenry, M.E., Ohkubo, T. & Hono, K. (2007). Structural studies of secondary crystallization products of the Fe23B6-type in a nanocrystalline FeCoB-based alloy. *J Appl Phys* **101**(9), 09N114.

MacLaren, J.M., Schulthess, T.C., Butler, W.H., Sutton, R. & McHenry, M. (1999). Electronic structure, exchange interactions, and curie temperature of FeCo. *J Appl Phys* **85**(8), 4833–4835.

Martin, Y. & Wickramasinghe, H.K. (1987). Magnetic imaging by force microscopy with 1000-a resolution. *Appl Phys Lett* **50**(20), 1455–1457.

McCartney, M.R. & Smith, D.J. (2007). Electron holography: Phase imaging with nanometer resolution. *Annu Rev Mater Res* **37**, 729–767.

McHenry, M.E., Willard, M.A., Iwanabe, H., Sutton, R.A., Turgut, Z., Hsiao, A. & Laughlin, D.E. (1999*a*). Nanocrystalline materials for high temperature soft magnetic applications: A current prospectus. *B Mater Sci* **22**(3), 495–501.

McHenry, M.E., Willard, M.A. & Laughlin, D.E. (1999*b*). Amorphous and nanocrystalline materials for applications as soft magnets. *Prog Mater Sci* **44**(4), 291–433.

Ohodnicki, P.R., Qin, Y.L., McHenry, M.E., Laughlin, D.E. & Keylin, V. (2010). Transmission electron microscopy study of large field induced anisotropy $(Co_{1-x}Fe_x)_{(89)}Zr_7B_4$ nanocomposite ribbons with dilute Fe-contents. *J Magn Magn Mater* **322**(3), 315–321.

Ping, D.H., Wu, Y.Q., Hono, K., Willard, M.A., McHenry, M.E. & Laughlin, D.E. (2001). Microstructural characterization of $(Fe_{0.5}Co_{0.5})_{(88)}Zr_7B_4Cu_1$ nanocrystalline alloys. *Scripta Mater* **45**(7), 781–786.

Pozzi, G. (2002). Electron holography of long-range electromagnetic fields: A tutorial. *Adv Imag Elect Phys* **123**, 207–223.

Saenz, J.J., Garcia, N., Grutter, P., Meyer, E., Heinzelmann, H., Wiesendanger, R., Rosenthaler, L., Hidber, H.R. & Gunterodt, H.J. (1987). Observation of magnetic forces by the atomic force microscope. *J Appl Phys* **62**(10), 4293–4295.

Shen, S., DeGeorge, V., Ohodnicki, P.R., Kernion, S.J., Keylin, V., Huth, J.F. & McHenry, M.E. (2014). Induced anisotropy in FeCo-based nanocomposites: Early transition metal content dependence. *J Appl Phys* **115**(17), 17A335.

Shindo, D. & Oikawa, T. (2002). *Analytical Electron Microscopy for Materials Science*. Tokyo; Berlin: Springer.

Shindo, D., Park, Y.G. & Yoshizawa, Y. (2002). Magnetic domain structures of $Fe_{73.5}Cu_1Nb_3Si_{13.5}B_9$ films studied by electron holography. *J Magn Magn Mater* **238**(1), 101–108.

Snoeck, E., Gatel, C., Lacroix, L.M., Blon, T., Lachaize, S., Carrey, J., Respaud, M. & Chaudret, B. (2008). Magnetic configurations of 30 nm iron nanocubes studied by electron holography. *Nano Lett* **8**(12), 4293–4298.

Tanigaki, T., Inada, Y., Aizawa, S., Suzuki, T., Park, H.S., Matsuda, T., Taniyama, A., Shindo, D. & Tonomura, A. (2012). Split-illumination electron holography. *Appl Phys Lett* **101**(4), 043101.

Tonomura, A. (1999). *Electron Holography*. Berlin; New York: Springer.

Yoshizawa, Y., Oguma, S. & Yamauchi, K. (1988). New Fe-based soft magnetic-alloys composed of ultrafine grain-structure. *J Appl Phys* **64**(10), 6044–6046.